Article

Optical Chirality Determined from Mueller Matrices

Hans Arwin [1,*], Stefan Schoeche [2], James Hilfiker [2], Mattias Hartveit [3], Kenneth Järrendahl [1], Olga Rubi Juárez-Rivera [4], Arturo Mendoza-Galván [4] and Roger Magnusson [1]

[1] Materials Optics, Department of Physics, Chemistry and Biology, Linköping University, SE-58183 Linköping, Sweden; kenneth.jarrendahl@liu.se (K.J.); roger.magnusson@liu.se (R.M.)
[2] J. A. Woollam Co., Inc., 645 M Street, Suite 102, Lincoln, NE 68508, USA; sschoeche@jawoollam.com (S.S.); jhilfiker@jawoollam.com (J.H.)
[3] Department of Chemical Engineering, University of Rochester, 4510 Wegmans Hall, P. O. Box 270166, Rochester, NY 14627-0166, USA; mhartvei@u.rochester.edu
[4] Cinvestav-Querétaro, Libramiento Norponiente 2000, Querétaro 76230, Mexico; olga.juarez@cinvestav.mx (O.R.J.-R.); amendoza@cinvestav.mx (A.M.-G.)
* Correspondence: hans.arwin@liu.se

Featured Application: The analysis of the transmission of Mueller matrices facilitates studies of optical activity in samples that also exhibit linear anisotropy and depolarization and may have a multilayered structure. Such studies are important for the development of applications in chiroptics.

Abstract: Optical chirality, in terms of circular birefringence and circular dichroism, is described by its electromagnetic and magnetoelectric material tensors, and the corresponding optical activity contributes to the Mueller matrix. Here, spectroscopic ellipsometry in the spectral range 210–1690 nm is used to address chiral phenomena by measuring Mueller matrices in transmission. Three approaches to determine chirality parameters are discussed. In the first approach, applicable in the absence of linear polarization effects, circular birefringence and circular dichroism are evaluated directly from elements of a Mueller matrix. In the second method, differential decomposition is employed, which allows for the unique separation of chirality parameters from linear anisotropic parameters as well as from depolarization provided that the sample is homogeneous along the optical path. Finally, electromagnetic modeling using the Tellegen constitutive relations is presented. The last method also allows structural effects to be included. The three methods to quantify optical chirality are demonstrated for selected materials, including sugar solutions, α-quartz, liquid crystals, beetle cuticle, and films of cellulose nanocrystals.

1. Introduction

Mueller matrices are increasingly used for the analysis of bianisotropic properties of complex media, including the quantification of circular birefringence (CB) and circular dichroism (CD). Traditionally, chiral parameters are studied by CD-spectroscopy and optical rotatory dispersion (ORD) methods. The purpose here is to discuss how Mueller-matrix analysis can complement the established methods by providing additional analytic features. Of special significance is that access to a full Muller matrix allows for the separation of circularly polarizing effects from linear birefringence (LB) and linear dichroism (LD). Furthermore, both CB and CD are accessible simultaneously from a Mueller matrix providing consistency checks through Kramers–Kronig analysis.

If a sample is depolarizing, the differential decomposition of a Mueller matrix can be employed to separate out depolarization so that it will not distort the analysis of chirality or linearly polarizing effects. However, the sensitivities obtainable with CD-spectroscopy

or ORD are not reached with commercially available Mueller-matrix ellipsometers. Still, the Mueller-matrix methodology is an important complement. To facilitate a comparison among different approaches, the use of transmission Mueller matrices to determine the chirality in samples is briefly reviewed and examples of data analysis from liquid and solid homogeneous as well as structured samples are discussed.

Methodology based on optical activity is used as a standard technique in many fields of science. Optical rotatory dispersion (ORD) is used in polarimetry to determine the concentrations of sugar-based solutions and also finds frequent use to determine chiral purity, e.g., for the separation of enantiomers in chemistry during drug development. Essentially, the magnitude and direction of rotation of polarized light is measured, often at a single wavelength, and related to molecular properties.

The rotation can be relatively large—on the order of degrees—and is easy to record. ORD can also be used for the structural analysis of biomolecules; however, in most cases, CD spectroscopy is used as it is more sensitive, has better spectral resolution, and has less overlap of spectral features [1]. An example of structural studies is analysis of the amount of α-helices, β-sheets, and random coils in proteins. In CD spectroscopy, the change in ellipticity is measured, which, in most cases, is specified in units of degrees. It can be very small and on the order of millidegrees.

Both CB and CD are included in a Mueller matrix and can be extracted directly in the absence of linear birefringence and linear dichroism. If linear effects are also present, a differential decomposition can be used to separate linear and circular effects as proposed by Go [2] and further detailed by Azzam [3]. Later, Ossikovski included the separation of depolarization [4]. Even though the methodology was proposed long ago, it has been ignored in interpretation of Mueller matrices. More recently, Arteaga and Kahr determined CD and CB from spectroscopic Mueller matrices measured on nickel sulfate hexahydrate crystals [5].

Giant optical activity was observed in thin films of enantiopure squaraines with opposite handedness [6]. Optical activity originating from structural effects in beetle cuticles was determined together with LB and LD as well as depolarization [7]. Chiral nanocrystalline cellulose free-standing films exhibit both linear and circular anisotropy and can be resolved by the differential decomposition of Mueller matrices [8]. Optical activity is contained in the electro-magnetic and magneto-electric tensors in the Tellegen constitutive relations and can be analyzed with Kramers–Kronig consistent dispersion models using Mueller matrices from beetle cuticles [9].

The objective of this paper is to describe three methodologic approaches to extract CD and CB from spectral Mueller matrices. First, we show how to determine CD and CB directly from the elements of a Mueller matrix in the case when there is no linear anisotropy. Then follows a description of differential decomposition of a Mueller matrix to determine all bianisotropic effects, thus including both linear and circular effects.

The differential decomposition methodology can also separate out effects of depolarization such that the results are not distorted. Finally, we present methodology to analyze the CD and CB with electromagnetic modeling using the Tellegen constitutive relations and Mueller matrices. With this method, samples with both CD and CB as well as LB and LD can be analyzed. The methodologies are demonstrated for liquid, solid, and structured samples.

2. Materials and Methods

2.1. Samples and Sample Preparation

Anhydrous D-glucose (J. T. Baker Chemicals B. V., Landsmeer, The Netherlands) was dissolved in distilled water to a concentration of 0.25 g/mL. An α-quartz plate with a diameter of 12.5 mm and nominal thickness of 1 mm was purchased from Changchun Boxin Photoelectric Co., Ltd., Chang Chun, China. The actual thickness was measured with a caliper and found to be 1.075 ± 0.005 mm.

The liquid crystal sample consists of a cholesteric glassy liquid crystal (ChGLC) sandwiched between two 3-mm thick glass substrates coated with buffed polyimide layers. The ChGLC in this study was Bz3ChN synthesized using Scheme 1 in Wallace et al. [10]. The material was heated beyond its clearing temperature and degassed. The isotropic material was deposited on a buffed polyimide glass substrate.

The second glass substrate was placed on top, and a small force was applied to spread the ChGLC film to the thickness of 10 μm as determined by silica micro-rods. Upon slight cooling to below the clearing temperature, a shearing force was applied to the glass substrates to align the ChGLC along the polyimide. The device was thermally annealed for 2 h at 200 °C after which it was quenched. A mono-domain Bz3ChN film is capable of circularly polarizing light with a selective reflection band centered at 410 nm.

Specimens of the scarab beetle *Cetonia aurata* (Linnaeus, 1758) were collected just outside Linköping in Sweden. The inside of one of the elytra from each specimen was mechanically cleaned with a scalpel to remove the endocuticle for improved transmission. The thickness of the optical active part of a cuticle varies slightly from beetle to beetle and also from position to position on an elytron. A thickness value of 20 μm was found by scanning electron microscopy [7] and was used for the samples studied here.

The film of cellulose nanocrystals (CNC) was prepared with ashless filter paper (Whatman grade 40) as the source of cellulose. The paper was ground in a coffee mill 3 times, each for 35 s. The hydrolysis was performed with concentrated sulfuric acid (64 wt%) with a ratio of 8.75 mL of acid per gram of paper at 45 °C for 120 min. The reaction was stopped by adding distilled water at 4 °C using 10 times the volume of hydrolysis solution. After resting for 24 h in a refrigerator, the diluted solution was decanted, and the recovered slurry was centrifuged three times with distilled water at 9000 rpm for 10 min each.

The paste of cellulose nanocrystals was dialyzed against 3 L of distilled water changing the water every 24 h until a neutral pH was reached in the water. The final pH of the nanocrystals inside the dialysis membrane was in the range of 3–4. The concentration of CNC was determined gravimetrically, and a suspension with 1.5 wt% of CNC was prepared and mechanically dispersed at 9000 rpm for 10 min. The CNC suspension was stored for one month before the film was cast by pouring 2.5 mL of CNC suspension in a petri dish with a 3 cm diameter. The evaporation-induced self-assembly was performed at laboratory conditions. Mueller-matrix measurements were performed six months after preparation. A thickness of 20 μm was evaluated with scanning electron microscopy.

2.2. Instrumentation

Mueller-matrix spectroscopic ellipsometry (MMSE) data were recorded in transmission mode at normal incidence with a dual rotating compensator ellipsometer (RC2, J. A. Woollam Co., Inc., Lincoln, NE, USA) with a beam diameter of 3 mm in the spectral range of 210–1690 nm. Focusing probes to reduce the beam diameter to below 100 μm were used for the measurements on beetle elytra. Complementary measurements to measure incomplete (three rows only) Mueller matrices were performed with a rotating-analyzer ellipsometer equipped with a compensator (VASE, J. A. Woollam Co., Inc.).

For the measurements on the glucose solution, a glass cuvette with path length of 13.8 mm was used. The cuvette was made of 1-mm thick fused quartz. With an empty cuvette, normalized Mueller-matrix elements within ±0.005 of their nominal value (zero or unity of the identity matrix) were obtained in the spectral range of 300–1690 nm. Below 300 nm, deviations up to ±0.015 were seen in some elements at the shortest wavelengths. When the cuvette was filled with glucose solution, the transmitted irradiance was low for longer wavelengths, and only data in the spectral range 210–1000 nm are presented.

Data analysis was performed with CompleteEASE and WVASE (J. A. Woollam Co., Inc.). The latter program was employed for modeling using the Tellegen constitutive relations. Model data were fitted to experimental data using nonlinear regression whereby best fit parameter values and their confidence limits were obtained. The confidence limits are defined as $SCL_i\sqrt{MSE}$, where SCL_i is the standard 90% confidence limit for the fit

parameter i determined from the diagonal of the covariance matrix of the fit, and *MSE* is the mean-squared error. Differential decomposition was performed with MATLAB. The decomposition code included an unweighted five-point moving average filter for spectral filtering to reduce noise.

3. Theory

Circular anisotropy can be quantified by the difference between refractive indices N_l and N_r for left- and right-handed circularly polarized light, respectively, according to $\Delta N_{lr} = N_l - N_r = n_l - n_r + i(k_l - k_r)$, where n and k denote the real and imaginary part, respectively. For transmission through a sample with thickness d and at wavelength λ, we introduce $C = C_B + iC_D$ where C_B and C_D are defined in Table 1 [11]. Samples may also have linear birefringence and linear dichroism, which are described by $L = L_B + iL_D$ for the xy reference directions and $L' = L'_B + iL'_D$ for the $\pm 45°$ reference directions. L_B, L_D, L'_B, and L'_D are defined in Table 1 (See Appendix A.1 for sign conventions).

Table 1. Definitions of the fundamental optical properties in the **L**- and **m**-matrices.

Property	L-Matrix	m-Matrix
Circular birefringence	$C_B = \mu d$	$\mu = 2\pi(n_l - n_r)/\lambda$
Circular dichroism	$C_D = \delta d$	$\delta = 2\pi(k_l - k_r)/\lambda$
xy birefringence	$L_B = \eta d$	$\eta = 2\pi(n_x - n_y)/\lambda$
xy dichroism	$L_D = \beta d$	$\beta = 2\pi(k_x - k_y)/\lambda$
$\pm 45°$ birefringence	$L'_B = \nu d$	$\nu = 2\pi(n_{45} - n_{-45})/\lambda$
$\pm 45°$ dichroism	$L'_D = \gamma d$	$\gamma = 2\pi(k_{45} - k_{-45})/\lambda$

The interaction between polarized light and a sample is here modeled in the so called Stokes–Mueller formalism $\mathbf{S}_o = \mathbf{M}\mathbf{S}_i$, where $\mathbf{S}_o$ and $\mathbf{S}_i$ are Stokes vectors of the outgoing and incident light, respectively. The 4×1 matrix (the Stokes vector is formally a column matrix but is, by tradition, called a vector) $\mathbf{S}$ carries all information about irradiance and polarization including the degree of depolarization of a light beam. The 4×4 matrix $\mathbf{M}$ is called the Mueller matrix of the optical system. A more detailed description of the formalism can be found elsewhere [3,12]. In this work, we use normalized Mueller matrices, which means that all elements are divided by the total transmittance, which corresponds to the first element in the first row in a measured unnormalized Mueller matrix. The notation of the elements in $\mathbf{M}$ is given by

$$\mathbf{M} = \begin{bmatrix} 1 & m_{12} & m_{13} & m_{14} \\ m_{21} & m_{22} & m_{23} & m_{24} \\ m_{31} & m_{32} & m_{33} & m_{34} \\ m_{41} & m_{42} & m_{43} & m_{44} \end{bmatrix}. \tag{1}$$

Below, we discuss how optical activity data can be extracted from MMSE-data through three routes: (I) directly from elements of a Mueller matrix if the sample only has circular anisotropy, i.e., only CB and/or CD; (II) by using differential decomposition provided that the sample is homogeneous along the optical path; and (III) dispersion-model analysis using the Tellegen constitutive relations.

3.1. Method I: Evaluation of Optical Activity Directly from Mueller-Matrix Elements

This method works if a sample only exhibits CB and/or CD and is assumed to have no linear anisotropy or depolarization. The parameter C_B then corresponds to circular

retardation. In a pure CB sample, like a sugar solution, the Mueller matrix becomes that of a rotator, which rotates polarization by an angle $\alpha = C_B/2$ [12]

$$
\mathbf{M}_R = \begin{bmatrix} 1 & 0 & 0 & 0 \\ 0 & \cos C_B & \mp \sin C_B & 0 \\ 0 & \pm \sin C_B & \cos C_B & 0 \\ 0 & 0 & 0 & 1 \end{bmatrix}.
\tag{2}
$$

Different authors use different conventions, and, in Equation (2), the upper signs of the $\sin C_B$ terms correspond to the use of the physics convention with time dependence according to $e^{-i\omega t}$ whereas the lower signs correspond to the engineering convention using $e^{i\omega t}$. The signs also depend on the definition of C_B. We will use the definition in Table 1 based on the difference $n_l - n_r$ and not on $n_r - n_l$, which also is in frequent use.

The parameter C_D is related to circular diattenuation, and the corresponding Mueller matrix becomes that of a circular diattenuator (see Appendix A.1 for the derivation).

$$
\mathbf{M}_D = \frac{T_l + T_r}{2} \begin{bmatrix} 1 & 0 & 0 & \tanh C_D \\ 0 & \operatorname{sech} C_D & 0 & 0 \\ 0 & 0 & \operatorname{sech} C_D & 0 \\ \tanh C_D & 0 & 0 & 1 \end{bmatrix},
\tag{3}
$$

where T_l and T_r are the transmittances for left-handed and right-handed polarized light, respectively. We also note that $\tanh C_D = -(T_l - T_r)/(T_l + T_r)$.

In general, both CD and CB are present, and the full Mueller matrix becomes

$$
\mathbf{M}_C = \mathbf{M}_R \mathbf{M}_D = \begin{bmatrix} 1 & 0 & 0 & \tanh C_D \\ 0 & \operatorname{sech} C_D \cos C_B & \mp \operatorname{sech} C_D \sin C_B & 0 \\ 0 & \pm \operatorname{sech} C_D \sin C_B & \operatorname{sech} C_D \cos C_B & 0 \\ \tanh C_D & 0 & 0 & 1 \end{bmatrix},
\tag{4}
$$

where the prefactor $(T_l + T_r)/2$ in Equation (4) has been omitted for the normalization of $\mathbf{M}_C$. The matrices $\mathbf{M}_R$ and $\mathbf{M}_D$ commute, and thus the order of multiplication in Equation (4) does not matter. For small values of C_B and C_D, as is often the case in CD spectroscopy and ORD, we can utilize series expansions to approximate $\operatorname{sech} C_D \approx 1$, $\cos C_B \approx 1$, $\sin C_B \approx C_B$ and $\tanh C_D \approx C_D$. Furthermore, $C_B = 2\alpha$ where α is the rotation of polarization used in ORD. In addition, we have, from Equation (A12), that $C_D \approx 2\epsilon$. ϵ is named "ellipticity" in CD spectroscopy but should more correctly be called the ellipticity angle. With these approximations, Equation (4) reduces to [13]

$$
\mathbf{M}_C \approx \begin{bmatrix} 1 & 0 & 0 & C_D \\ 0 & 1 & \mp C_B & 0 \\ 0 & \pm C_B & 1 & 0 \\ C_D & 0 & 0 & 1 \end{bmatrix} = \begin{bmatrix} 1 & 0 & 0 & 2\epsilon \\ 0 & 1 & \mp 2\alpha & 0 \\ 0 & \pm 2\alpha & 1 & 0 \\ 2\epsilon & 0 & 0 & 1 \end{bmatrix}.
\tag{5}
$$

For small optical activity, ϵ and α are, thus, obtained directly from the secondary diagonal in Equation (5). In ORD applied to molecules in solution, the rotation is normalized by the optical path length d in dm and concentration c in g/cm^3 and specified at a certain wavelength and temperature T, and also converted from radians to degrees. The specific rotation is, then, obtained as

$$
[\alpha]_\lambda^T = \frac{\alpha}{dc}.
\tag{6}
$$

In standard reflection ellipsometry, the complex reflectance ratio is defined as $\rho = r_p/r_s = \tan \Psi e^{i\Delta}$, where $\tan \Psi = |r_p|/|r_s|$ and $\Delta = \arg r_p - \arg r_s$ with r_p and r_s denoting

the complex-valued reflection coefficients for p- and s-polarized light, respectively. We present an analogous chiral transmittance ratio ρ_C defined as in [14]

$$\rho_C = t_l/t_r = \tan \Psi_C e^{i\Delta_C} \tag{7a}$$

$$\tan \Psi_C = |t_l|/|t_r| = e^{-\frac{2\pi d}{\lambda}(k_l - k_r)} \tag{7b}$$

$$\Delta_C = \arg t_l - \arg t_r = \frac{2\pi d}{\lambda}(n_l - n_r), \tag{7c}$$

where $t_l = e^{\frac{2\pi d}{\lambda}i(n_l + ik_l)}$ and $t_r = e^{\frac{2\pi d}{\lambda}i(n_r + ik_r)}$ are the eigenpolarizations for left-handed and right-handed polarized light, respectively. If we also observe that $\sec C_D = \sin 2\Psi_C$, $C_B = \Delta_C$ and $\tanh C_D = -\cos 2\Psi_C$, we can rewrite Equation (4) as

$$\mathbf{M}_C = \begin{bmatrix} 1 & 0 & 0 & -\cos 2\Psi_C \\ 0 & \sin 2\Psi_C \cos \Delta_C & \mp \sin 2\Psi_C \sin \Delta_C & 0 \\ 0 & \pm \sin 2\Psi_C \sin \Delta_C & \sin 2\Psi_C \cos \Delta_C & 0 \\ -\cos 2\Psi_C & 0 & 0 & 1 \end{bmatrix}. \tag{8}$$

Equation (8) is applicable for samples exhibiting only optical activity and no linear anisotropic effects and can be used as an alternative to Equation (4).

3.2. Method II: Differential Decomposition

Method I is not directly applicable if a sample has both circular and linear anisotropic effects, as linear effects may mix with circular effects complicating the interpretation of the Mueller-matrix elements. In method II, a differential decomposition is employed whereby the natural logarithm of a normalized transmission Mueller matrix is calculated. For a non-depolarizing sample, we obtain [2,3,5]

$$\mathbf{L} = \ln \mathbf{M} = \begin{bmatrix} 0 & -L_D & -L_D' & C_D \\ -L_D & 0 & C_B & -L_B' \\ -L_D' & -C_B & 0 & L_B \\ C_D & L_B' & -L_B & 0 \end{bmatrix}. \tag{9}$$

The birefringent and dichroic properties are obtained directly from the elements of $\mathbf{L}$. For the result to be correct, the sample must be homogeneous along the optical path. The birefringence parameters are determined from the logarithm of exponential functions with arguments that are complex-valued. These functions are cyclic with a period of 2π. The parameters C_B, L_B and L_B' are, thus, obtained with an uncertainty of $N \cdot 2\pi$, where the order parameter $N(0, \pm 1, \pm 2, \dots)$ is an integer that depends on the optical path length, and the sign is that of the birefringence parameter.

The MATLAB algorithm delivers values confined to the range $\pm \pi$. The data can be unfolded to the correct order by an offset adjustment of $N \cdot 2\pi$, where N may be different in different spectral ranges as shown by Mendoza-Galván et al. [15]. An offset adjustment will be demonstrated in the analysis of the α-quartz sample in Section 4.2.

If the sample thickness d is known, the elementary intrinsic materials properties are obtained from the elements of the matrix $\mathbf{m} = \mathbf{L}/d$, e.g., $\eta = L_B/d = \frac{2\pi}{\lambda}(n_x - n_y)$ and similar for the other elements of $\mathbf{m}$ as specified in Table 1. If the sample is depolarizing, $\mathbf{L}$ becomes asymmetric and can be written as a sum of two matrices

$$\mathbf{L} = \mathbf{L}_m + \mathbf{L}_u, \tag{10}$$

where $\mathbf{L}_m$ is Minkowski antisymmetric and provides the birefringence and dichroic properties of the sample, whereas $\mathbf{L}_u$ is Minkowski symmetric and provides the depolarization properties. Further details are given by Ossikovski [4].

3.3. Method III: Modeling Using the Tellegen Constitutive Relations

An effective medium approach is used to determine effective chiral properties of a sample. The method is based on the Tellegen constitutive relations

$$\mathbf{D} = \varepsilon_0 \boldsymbol{\varepsilon} \mathbf{E} + c^{-1} \boldsymbol{\xi} \mathbf{H} \tag{11a}$$

$$\mathbf{B} = c^{-1} \boldsymbol{\zeta} \mathbf{E} + \mu_0 \boldsymbol{\mu} \mathbf{H}, \tag{11b}$$

where the electric displacement field $\mathbf{D}$, the electric field $\mathbf{E}$, the magnetic field $\mathbf{H}$, and the magnetic flux density $\mathbf{B}$ are interrelated by the materials tensor permittivity $\boldsymbol{\varepsilon}$, permeability $\boldsymbol{\mu}$, and the magnetoelectric tensors $\boldsymbol{\xi}$ and $\boldsymbol{\zeta}$. The vacuum permittivity and permeability are denoted as ε_0 and μ_0, respectively, and c is the vacuum speed of light. Notice that $\boldsymbol{\varepsilon}$ and $\boldsymbol{\mu}$ are defined in the xyz coordinate system. The tensor $\boldsymbol{\xi}$ can be expanded as $\boldsymbol{\xi} = \boldsymbol{\chi} + \mathrm{i}\boldsymbol{\kappa}$ where $\boldsymbol{\chi}$ and $\boldsymbol{\kappa}$ are the nonreciprocity tensor and chirality tensor, respectively. The materials studied here are reciprocal implying $\boldsymbol{\chi} = 0$, which leads to $\boldsymbol{\xi} = -\boldsymbol{\zeta}^{\mathrm{T}} = \mathrm{i}\boldsymbol{\kappa}$ where T indicates transposition [16].

In a transmission measurement at normal incident in a Cartesian xyz coordinate system, aligned with the instrument framework and with z being the direction of wave propagation, we do not probe the z-components of the material tensors. Furthermore, in the presence of biaxial anisotropy, the optical axes x' and y' of a sample may differ an angle ϕ (in-plane Euler angle) from the axes x and y. The samples studied here are either isotropic or have their helical axis along the z-direction, and the general form of the chirality tensor used is $\boldsymbol{\kappa} = \mathrm{diag}(\kappa_x, \kappa_y, \kappa_z)$.

Furthermore, $\kappa_x = \kappa_y$ and, as κ_z can be set arbitrarily, we can use $\kappa_x = \kappa_y = \kappa_z = \kappa$ and simplify to $\boldsymbol{\kappa} = \kappa \mathbf{I}$ where $\kappa = \kappa_{\mathrm{Re}} + \mathrm{i}\kappa_{\mathrm{Im}}$ is a complex-valued scalar representation of chirality and $\mathbf{I}$ is the identity matrix. The permittivity tensor is assumed to be diagonal $\boldsymbol{\varepsilon}_{x'y'} = \mathrm{diag}(\varepsilon_{x'}, \varepsilon_{y'}, \varepsilon_z)$. Its elements are related to the refractive index by $N_j = n_j + \mathrm{i}k_j = \sqrt{\bar{\varepsilon}_j}$ ($j = x', y', z$). In transmission ellipsometry at normal incidence, the absolute phase is not accessible, and there is no sensitivity to the absolute values of $n_{x'}$ and $n_{y'}$. However, the difference $\Delta n_{x'y'} = n_{x'} - n_{y'}$ can be evaluated.

With normalized Mueller matrices as used here, we also lose sensitivity to isotropic absorption; however, $\Delta k_{x'y'} = k_{x'} - k_{y'}$ can be determined. As ε_z can be set arbitrarily, we use $\boldsymbol{\varepsilon} = \mathbf{A}_{\mathrm{E}} \mathrm{diag}(N_{x'}^2, (N_{x'} - \Delta n_{x'y'} - \mathrm{i}\Delta k_{x'y'})^2, N_{x'}^2) \mathbf{A}_{\mathrm{E}}^{-1}$, where $\mathbf{A}_{\mathrm{E}}$ is the Euler rotation matrix with only the in-plane rotation angle $\phi \neq 0$. Equation (11) can now be reformulated as

$$\mathbf{D} = \varepsilon_0 \mathbf{A}_{\mathrm{E}} \mathrm{diag}(N_x^2, (N_x - \Delta n + \mathrm{i}\Delta k)^2, N_x^2) \mathbf{A}_{\mathrm{E}}^{-1} \mathbf{E} + c^{-1} \mathrm{i}\kappa \mathbf{H} \tag{12a}$$

$$\mathbf{B} = -c^{-1} \mathrm{i}\kappa \mathbf{E} + \mu_0 \mathbf{H}, \tag{12b}$$

where $\mu = \mathbf{I}$ is assumed. The choices of dispersion models for κ, Δn, and Δk depend on the material and are described separately for each material in the Results section.

For the propagation of electromagnetic plane waves in chiral media, the allowed solutions include κ in the refractive indices according to [17].

$$N_{\mathrm{l}} = \sqrt{\varepsilon \mu} - \kappa \tag{13a}$$

$$N_{\mathrm{r}} = \sqrt{\varepsilon \mu} + \kappa. \tag{13b}$$

This leads to $2\kappa = N_{\mathrm{r}} - N_{\mathrm{l}}$, i.e., $2(\kappa_{\mathrm{Re}} + \mathrm{i}\kappa_{\mathrm{Im}}) = n_{\mathrm{r}} - n_{\mathrm{l}} + \mathrm{i}(k_{\mathrm{r}} - k_{\mathrm{l}})$. Combined with the definitions in Table 1, we find

$$C_{\mathrm{B}} = -\frac{4\pi d}{\lambda} \kappa_{\mathrm{Re}} \tag{14a}$$

$$C_{\mathrm{D}} = -\frac{4\pi d}{\lambda} \kappa_{\mathrm{Im}}. \tag{14b}$$

The chirality parameter κ is, thus, useful for the determination of rotation $\alpha = C_B/2$ in ORD and for ellipticity ϵ using Equation (A5) in the general case or using $\epsilon \approx C_D/2$ (Equation (A12)) for a small dichroism in CD spectroscopy.

4. Results

Applications of the three methods above on samples with different complexity from different materials classes are demonstrated. The first sample is a solution of D-glucose, which is biisotropic and only exhibits CB. The second sample is solid α-quartz, which also only exhibits CB. The next sample is a beetle cuticle, which is structured. Its twisted lamellar structure acts as a circular Bragg filter. Then, we explore a cholesteric liquid crystal, which in addition to CB, also acts as a circular Bragg filter with both CB and CD in a narrow spectral band. Finally, a film of cellulose nanocrystals is analyzed, which is structured but with more complexity than the beetle cuticle.

4.1. Optical Activity in Solution: Glucose

A water solution of glucose is biisotropic and is, here, included as an introductory example of a medium with circular birefringence and with all other optical properties being scalars. Figure 1 shows a transmission Mueller matrix for a water solution of D-glucose. This sample has only CB, which is confirmed by the Mueller matrix as it is of the form in Equation (2).

4.1.1. Method I

In method I we calculate the average (The minus sign on m_{32} and plus sign on m_{23} is because the instrument used delivers data based on the $e^{i\omega t}$ convention.) of m_{23} and $-m_{32}$ in Figure 1. We find that $\sin C_B = \sin 2\alpha = 0.06317$ at 589 nm, which, with a concentration of 0.25 g/mL and a path length of 0.138 dm in Equation (6), gives a specific rotation $[\alpha]^{20}_{589} = +52.5 \, [\text{deg} \, \text{dm}^{-1} \, \text{cm}^3 \, \text{g}^{-1}]$.
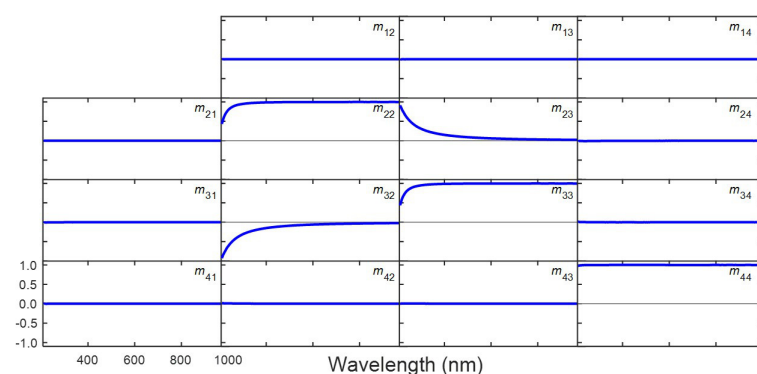

Figure 1. The transmission Mueller matrix of a D-glucose solution.

4.1.2. Method II

In method II, we apply a differential decomposition to the data in Figure 1 with the results presented in Figure 2, which confirms that the linear effects L_B, L_D, L'_B, and L'_D are very small. At $\lambda = 589$ nm, we find $C_B = 0.06318$ rad, which corresponds to $[\alpha]^{20}_{589} = +52.5 \, [\text{deg} \, \text{dm}^{-1} \, \text{cm}^3 \, \text{g}^{-1}]$.
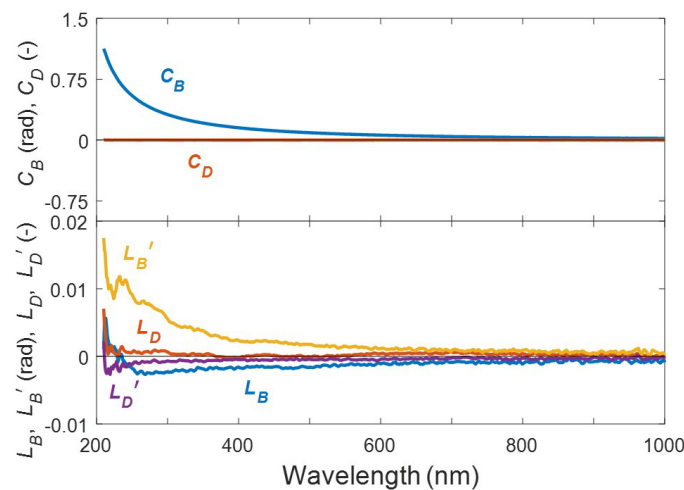
Figure 2. Birefringence and dichroism determined by differential decomposition of the MMSE data for the D-glucose solution in Figure 1. Observe the expanded scale for L_B, L_D, L_B' and L_D'.

4.1.3. Method III

In method (III), a real-valued κ is modeled with a Cauchy model function. With λ given in μm, it is defined by

$$\kappa = A + \frac{B}{\lambda^2} + \frac{C}{\lambda^4} + \frac{D}{\lambda^6}. \tag{15}$$

Figure 3 shows the Cauchy model spectra for κ of the D-glucose solution fitted to the normalized Mueller matrix in Figure 1 using Equation (12). In the fit, we set $\Delta n = \Delta k = 0$ as the solution is isotropic, and N_x was arbitrarily set to 1.33 + i0 as there is no sensitivity to the absolute phase and isotropic absorption in a normal incidence transmission measurement. The values of the Cauchy parameters are shown in Table 2. Finally, we can calculate $[\alpha]_{589}^{20}$. From Figure 3, we have $\kappa_{\text{Re}} = 2.128 \times 10^{-7}$ at $\lambda = 589$ nm and from Equation (14a), we obtain $[\alpha]_{589}^{20} = +52.0$ [deg dm^{-1} cm^3 g^{-1}].
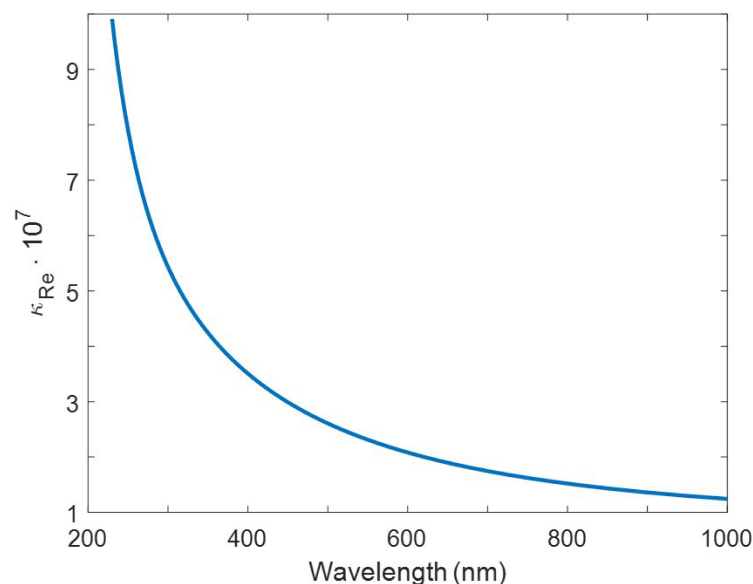

Figure 3. Model function for the chirality κ of a D-glucose solution.

Table 2. Cauchy parameters for κ-fits for D-glucose and α-quartz. Values in parenthesis are the confidence limits in the last decimal.

Sample	A (-)	B (μm^2)	C (μm^4)	D (μm^6)
D-glucose	$7.24 \times 10^{-8}(8)$	$5.41 \times 10^{-8}(4)$	$-2.14 \times 10^{-9}(6)$	$9.8 \times 10^{-11}(2)$
α-quartz	$7.27 \times 10^{-6}(2)$	$1.771 \times 10^{-5}(2)$	$9.62 \times 10^{-7}(3)$	$-7.10 \times 10^{-9}(6)$

4.2. Optical Activity in Solids: α-Quartz

4.2.1. Method I

Measurements on an α-cut quartz crystal are included as an example of a solid with only circular birefringence. A transmission Mueller matrix measured on a sample with a nominal thickness of 1 mm is shown in Figure 4. The profound oscillations in elements m_{22}, m_{23}, m_{32}, and m_{33} indicate that the rotation of polarization is larger than that of the glucose solution. The polarization effects are confined to these four elements showing that the sample is a circular diattenuator (rotator).

The remaining elements differ less than 0.002 from their expected values of zero or unity in most of the spectral range but with deviations up to 0.01 for shorter wavelengths in some elements. From the data in Figure 4, we have $(m_{23} - m_{32})/2 = 0.727$ at $\lambda = 589$ nm. If we use Equation (2), we find the rotation angle $\alpha = \arcsin(0.727)/2 = 23.32°$, and, if we use the reference value of 21.73° [18], we obtain a sample thickness of $d = 23.32°/21.73°$ mm= 1.073 mm.
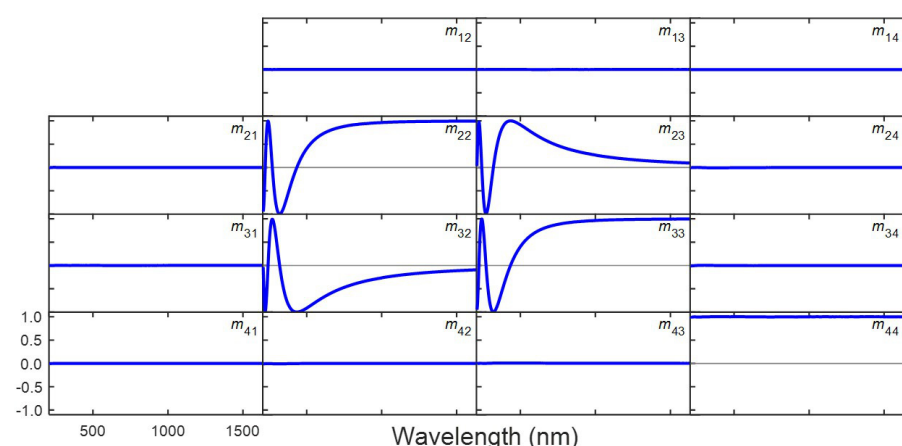
Figure 4. The transmission Mueller matrix of an α-cut quartz sample.

4.2.2. Method II

Figure 5 shows C_B from a differential decomposition of the data in Figure 4. The circular dichroism C_D is very close to zero, and all linear effects L_B, C_B, L'_B and C'_B are small ($<10^{-2}$ for $\lambda > 300$ nm) and are not shown. Observe that the solid curve for short wavelengths shows C_B offset-adjusted by 2π to provide first-order values, whereas the dashed curve shows the unfolded data from the decomposition. At $\lambda = 589$ nm, we find $C_B = 0.8143$ rad, which corresponds to a rotation of 23.33°, and, with a specific rotation of α-quartz equal to 21.73° [18], we find a thickness of 1.074 mm. As a second test, we use $C_B = 2.204$ rad at $\lambda = 373$ nm and with a specific rotation of 58.89° [18], we find a thickness of 1.073 mm.
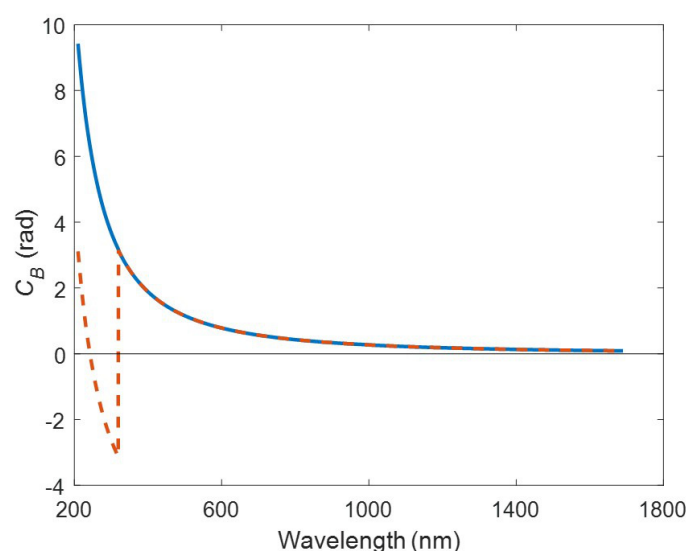
Figure 5. The birefringence C_B (solid curve) for an α-quartz sample determined by differential decomposition of the MMSE data in Figure 4. The dashed curve shows unfolded C_B as obtained from the differential decomposition.

4.2.3. Method III

In a similar way as for the D-glucose results, we fitted the α-quartz Mueller matrix to Equation (12) using the Cauchy model in Equation (15) for κ with results as in Table 2. The fit is of similar quality as for the D-glucose solution and is not shown.

4.3. *Structural Optical Activity in Cuticle from Cetonia Aurata*

Several beetles in the Scarabaeoidea superfamily have circular Bragg reflectors in their cuticle [19]. The phenomenon was observed in 1911 by Michelson [20] and has been studied extensively by several methods. A review with a focus on biomimetics is given by Lenau and Barfoed [21]. During the last decade, Mueller-matrix studies on beetle cuticles have been introduced by Goldstein [22], Hodgkinson [23] and our group [7,9,24–28].

4.3.1. Method I

Figure 6 shows transmission Mueller matrices from elytra from two specimens of the scarab beetle *Cetonia aurata*. Beetles are individuals and exhibit differences in their optical features, and data from one specimen with small depolarization (sample CA1) and one with large depolarization (sample CA2) are shown. The depolarization of the two samples are shown in Figures S1–S3 in Supplementary Materials. A common feature is that right-handed circularly polarized light is transmitted in a band around 550 nm as seen in the elements m_{41} and m_{14} indicating circular dichroism. Corresponding circular birefringence features are seen in elements m_{32} and m_{23}.

Contributions from CD and CB are also observed in elements m_{22} and m_{33} in accordance with Equation (4). The non-zero but small values of $m_{31} = m_{13}$ and $m_{42} = m_{24}$ show, however, that the elytra has some linear polarization effects. In fact, the elytra are biaxial as revealed by analysis of Mueller matrices measured in reflection mode [26]. If the Mueller matrices in Figure 6 are compared with Equation (4), we can make the qualitative conclusion that the cuticle from these beetles exhibits chirality with a resonance and transmits right-handed circularly polarized light in the spectral band 500–600 nm. Due to the complex structure, a quantitative analysis using method I is not recommendable.
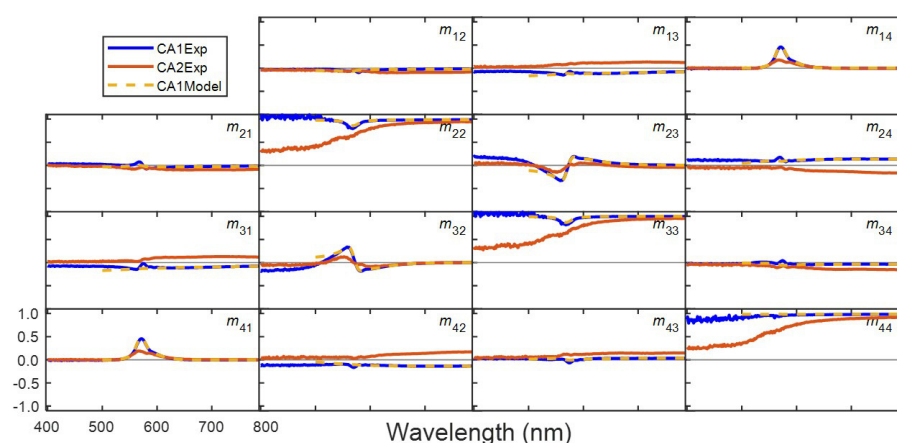
Figure 6. Transmission Mueller matrices of elytra from two specimens of *C. aurata*. The blue and red solid curves are data recorded on specimens with low (sample CA1) and high (sample CA2) depolarization, respectively. The yellow dashed curve is the best fit to data from CA1 using regression analysis in a bianisotropic model (method III).

4.3.2. Method II

Differential decompositions of the data in Figure 6 are shown in Figures 7 and 8 and reveal the bianisotropic properties. The circular effects C_B and C_D dominate but some linear effects are seen. Sample CA1 has larger optical activity with a maximum of $C_D = 0.5$ compared to sample CA2 with a maximum of $C_D = 0.38$. Sample CA1 has an azimuth such that the biaxial properties are close to the $\pm 45°$ direction of the instrument reference coordinate system resulting in small L_B and L_D, and most of the information about linear anisotropy is found in L'_B and L'_D. In sample CA2, linear birefringence and dichroism are distributed between L_B and L'_B and L_D and L'_D, respectively, due to another azimuth. Sample CA2 has larger depolarization compared to sample CA1 as seen in the $\mathbf{L}_u$-matrices in Supplementary Materials.
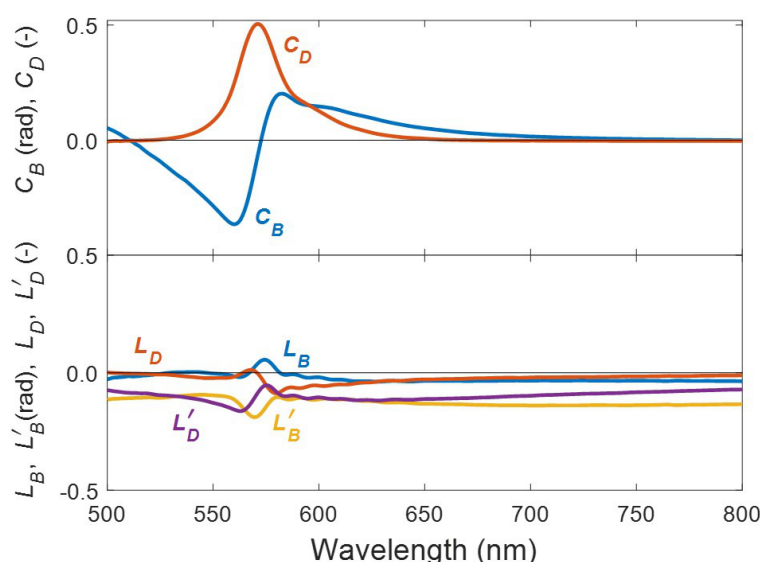

Figure 7. Birefringence and dichroism of the elytron from *C. aurata* (sample CA1).
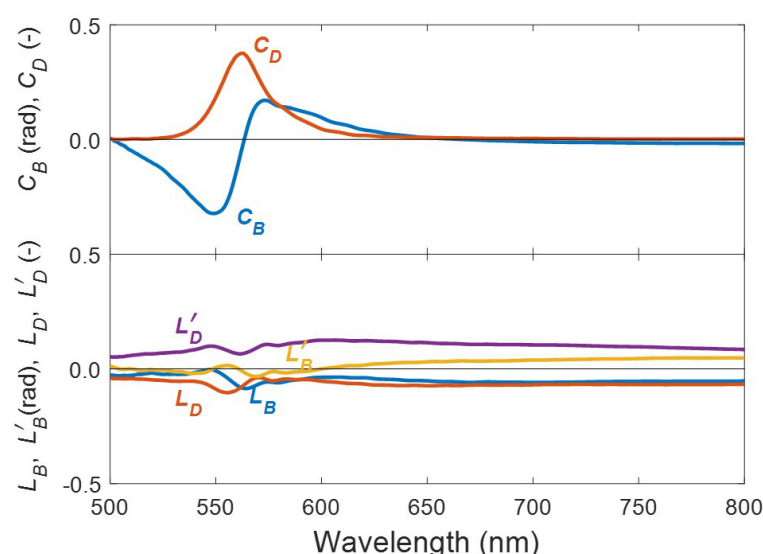
Figure 8. Birefringence and dichroism of the elytron from *C. aurata* (sample CA2).

4.3.3. Method III

The Mueller matrix from sample CA1 was used in nonlinear fitting whereby the index difference $\Delta N_{x'y'} = \Delta n_{x'y'} + i\Delta k_{x'y'}$ and the chirality $\kappa = \kappa_{\text{Re}} + i\kappa_{\text{Im}}$ in Equation (12) were fitted in a single layer model with film thickness 20 μm and with dispersion models for the optical functions. Two Gaussian resonances were used for κ according to

$$\kappa_{\text{Im}}(E) = \sum_{j=1}^{2} \left[A_j e^{-\left(\frac{E-E_{0j}}{\Gamma_j}\right)^2} - A_j e^{-\left(\frac{E+E_{0j}}{\Gamma_j}\right)^2} \right] \tag{16a}$$

$$\kappa_{\text{Re}}(E) = \kappa_0 + \text{KK}(\kappa_{\text{Im}}), \tag{16b}$$

where A_j, E_{0j}, and Γ_j are the amplitude, resonance energy, and broadening of resonance j, respectively. κ_0 is a constant, and KK stands for a Kramers–Kronig transform. In Equation (16), the spectral dependences are expressed versus the photon energy $E = hc/\lambda$ (in units of eV), where h is Planck's constant. Details about modeling the linear properties are found elsewhere [9]; however, in brief, linear birefringence $\Delta n_{x'y'}$ is fitted with a Cauchy expression similar to that in Equation (15) but with only three terms, and a small linear dichroism $\Delta k_{x'y'}$ is fitted with an exponential term, a so-called Urbach tail [9].

The sample optical axes are not aligned to the reference axes x and y of the instrument, and a Euler rotation angle ϕ is included in the fit, and a value $\phi = -52.4°$ was found. This is close to $\phi = -45°$ explaining why L'_{B} and L'_{D} are larger compared to L_{B} and L_{D}.

In Figure 9, the chirality parameter κ as obtained by regression and with best-fit parameters as given in Table 3 is shown. The asymmetry seen in m_{41} and m_{14} and in C_{D} in Figure 6 is clearly revealed in κ_{Im} in Figure 9 and is reasonably modeled with the two overlapping Gaussian resonances. The physical origin of the double resonance might be a chiral structure with a gradient in pitch throughout the sample or with two different pitches at different depths. An attempt to model the Mueller-matrix data from specimen CA2 using regression analysis failed as the large depolarization could not be reproduced.

Table 3. Gaussian parameters and corresponding confidence limits for κ for the cuticle of *C. aurata* (sample CA1).

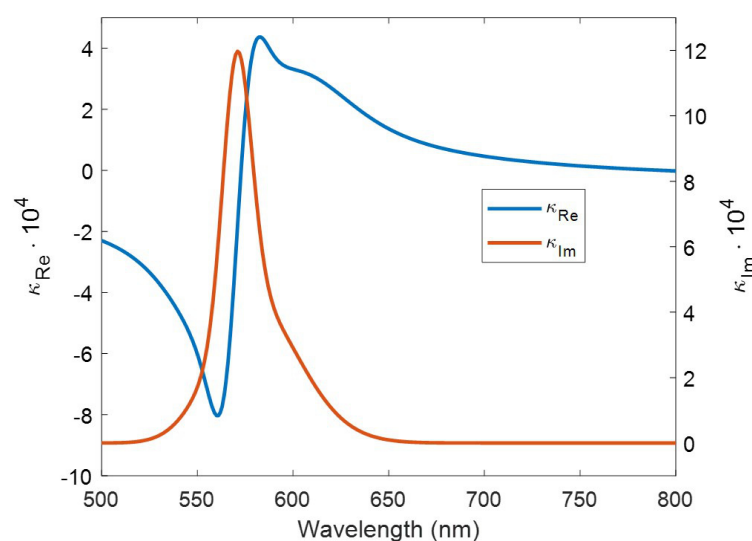| Resonance	A_j (-)	E_{0j} (eV)	Γ_j (eV)
1	0.00042 ± 0.00002	2.138 ± 0.003	0.197 ± 0.004
2	0.00081 ± 0.00002	2.173 ± 0.001	0.066 ± 0.002

Figure 9. Model function with two Gaussian resonances for the chirality parameter κ of the elytron from *C. aurata* (sample CA1).

4.4. Optical Activity in Liquid Crystals

Figure 10 shows the transmission Mueller matrix of the ChGLC sample. A circular Bragg resonance that transmits right-handed circularly polarized light with strong circular dichroism is observed in the elements m_{41} and m_{14}, which are very close to each other. The resonance is centered at 409 nm with a width at half maximum of $\approx$120 nm. The corresponding circular birefringence is found in the four central elements analogous to the quartz sample data in Figure 4. A major difference is that the quartz sample did not exhibit any circular dichroism, whereas this was the case for the ChGLC sample due to the Bragg resonance.

Furthermore, the circular dichroism is so strong that it masks the circular birefringence in the Bragg window. This is an effect of that large values of C_D that cause sech C_D to be close to zero and, thereby, down-weight the C_B contributions as found by inspection of Equation (4). This effect also causes the damping of the oscillations in the four central elements for wavelengths close to but outside the Bragg window when sech C_D decreases from unity far from the resonance to zero in the Bragg resonance. The elements m_{12}, m_{13}, m_{21}, m_{24}, m_{31}, m_{34}, m_{42}, and m_{43} are close to zero indicating a very small linear anisotropy.
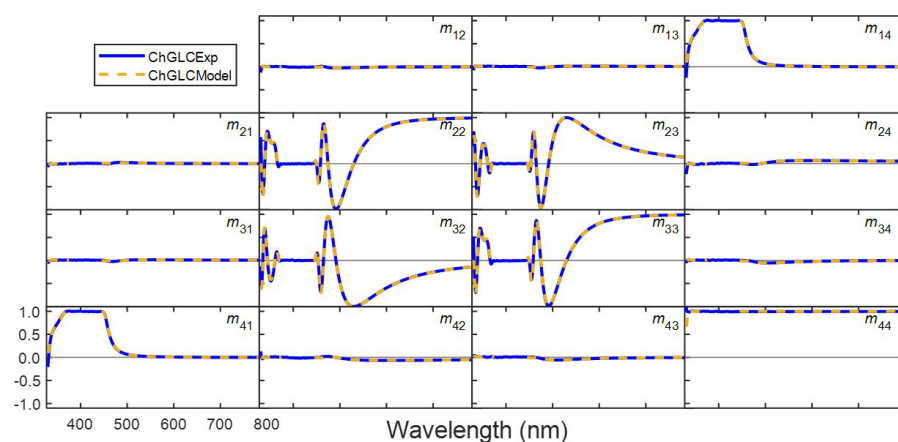

Figure 10. Transmission Mueller matrix of the ChGLC sample (solid curve) and the best fit obtained using Equation (12) (dashed curves).

4.4.1. Method I

In the Bragg band, the sample is a circular polarizer as seen in Figure 11. Elements m_{41} and m_{14} are close to unity, but the experimental resolution is not sufficient to make a meaningful determination of C_D as $\tanh C_D$ has an exponential dependence on C_D. Similarly, C_B is not accessible. For wavelengths sufficiently far from the Bragg band, when $\tanh C_D \approx 0$ and $\mathrm{sech}\, C_D \approx 1$, the sample represents a circular retarder as seen in Figure 10 for $\lambda > 450$ nm. If we, for example, select $\lambda = 600$ nm, we obtain a rotation angle of $\alpha = 18.23°$ from the average of $C_B/2$ in the elements m_{23} and m_{32}.
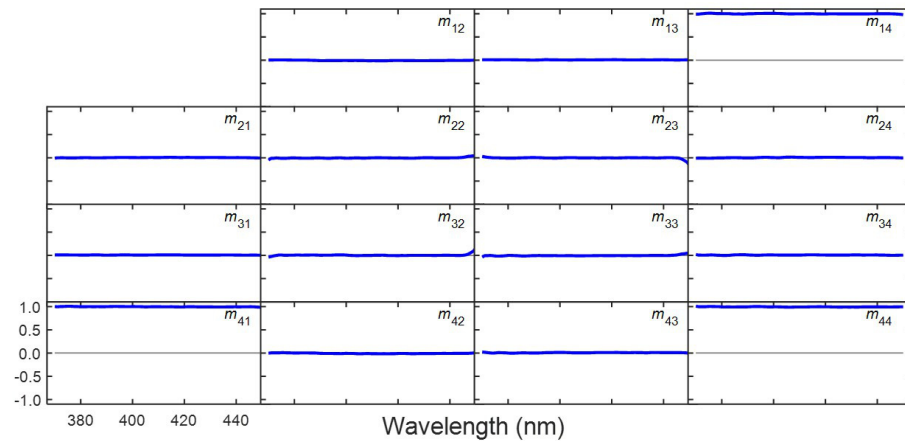

Figure 11. Transmission Mueller matrix of the ChGLC sample in the Bragg band.

4.4.2. Method II

Figure 12 shows C_B and C_D from a differential decomposition of the data in Figure 10. The linear effects L_B, C_B, L'_B, and C'_B are small and are not shown. In the Bragg band between 365 nm and 450 nm, m_{41} and m_{14} are close to unity due to the large circular dichroism. Ideally, these elements should asymptotically approach $+1$ or -1, for right- and left-handed polarization, respectively, if the number of periods in the twisted layer becomes large.

However, if we recall that $m_{41} = \tanh C_D = (e^{C_D} - e^{-C_D})/(e^{C_D} + e^{-C_D})$, which corresponds to $C_D = \ln\left[(1 + m_{41})/(1 - m_{41})\right]$, we notice that, for m_{41} close to $+1$ or -1, the accuracy in C_D becomes low (Similar reasoning also holds for m_{14}). Due to the limited resolution and noise ($|m_{41}|$ and $|m_{14}|$ can even be >1 at some wavelengths), differential decomposition can not resolve C_D accurately in the Bragg band explaining the noise in C_D in Figure 12.

For C_B, we observe that, when it approaches the Bragg resonance from the long wavelength side, it increases rapidly but becomes inaccessible in the Bragg band as the left-handed component becomes completely attenuated and the transmitted light is right-handed circularly polarized. The anomalous rotatory dispersion in the Bragg band can, thus, not be seen as is the case in other experimental data on liquid crystals with lower optical activity [29] as well as in the cuticle data in the previous section and for CNC in the next section.

Observe that C_B is offset adjusted (see Section 3.2) with the order parameter N to provide correct values. Also notice that the value of C_B is uncertain with $N \cdot 2\pi$ on the short wavelength side as the order parameter N cannot be determined. However, to align C_B with the results obtained with Method III (see below), an offset adjustment with $N = -11$ is done in Figure 12. The match is perfect.
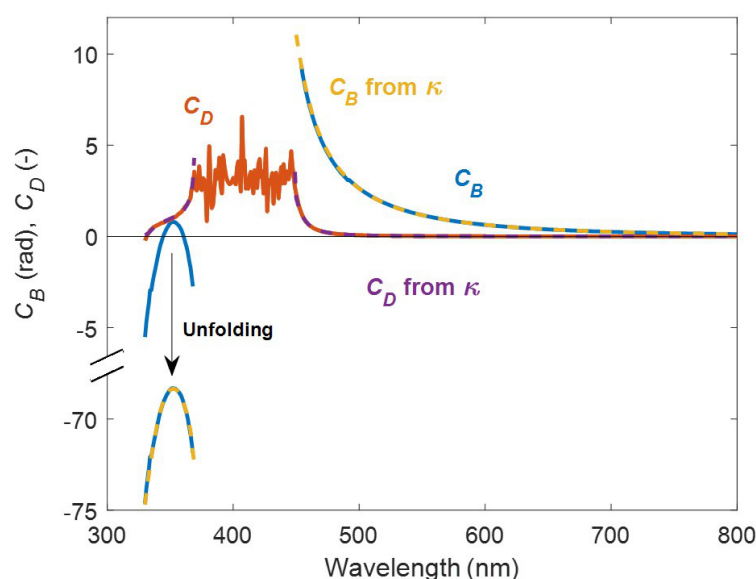
Figure 12. Circular dichroism C_D and circular birefringence C_B for the ChGLC sample determined by differential decomposition of the MMSE data in Figure 10 (solid curves). An offset adjusted curve ("Unfolding", see text for details) for C_B is also shown. The dashed curves show C_B and C_D calculated from fitted κ.

4.4.3. Method III

It was found that the chirality parameter κ could not be fitted over the full experimental spectral range when using Method III. The linear regression failed in the Bragg band. However, for wavelengths larger than 450 nm, a combination of Gaussian oscillators and Cauchy terms were used to model κ, $\Delta n_{x'y'}$, and $\Delta k_{x'y'}$ in Equation (12). For wavelengths shorter than 375 nm, the experimental data could be modeled but the model fits to the data for the ChGLC sample should only be considered as mathematical fits, and a physical interpretation of Gaussian resonance energies, etc. is of limited value. The model fits are shown in Figure 10.

The obtained model data represent the bianisotropic optical properties of the sample and allow C_B and C_D to be calculated from Equation (14) as shown in Figure 12. For wavelengths larger than the Bragg band, both C_B and C_D are in very good agreement with the corresponding data obtained with Method II. This also holds for C_D for wavelengths shorter than the Bragg band, whereas the C_B data from Method III are much more negative than those obtained from Method II.

The curvature of C_B for short wavelengths may be an artifact due to that the transmission drops below 350 nm, which may induce systematic errors. Another more interesting possibility is that dispersion in ChGLC optical properties may generate additional Bragg resonances [30,31]. The large offset in C_B leads to values of the order -65 rad as seen in Figure 12. This corresponds to a rotation of polarization $\alpha = C_B/2 \approx 1800°$ or, if normalized to the 10 μm thickness, to 180,000°/mm. This appears surprisingly large, but liquid crystals may have very high rotatory power, even hundreds of revolutions per mm [32]. Even larger rotations have been observed in 20-nm thin films of squaraine, where a maximum in $C_B = 0.2$ rad corresponds to a rotation approaching $3 \times 10^{5°}$ [6].

4.5. *Structural Optical Activity in Cellulose Nanocrystals*

As a final example, we discuss some preliminary studies on a freestanding film of CNC. The film structure is more complex, exhibits a mixture of chiral and non-chiral anisotropic phases, and is polydomain. The distribution of pitch and helical axis orientations is also ubiquitous.

4.5.1. Method I

Figure 13 shows the transmission Mueller matrix of a CNC film; however, no quantification using method I is meaningful due to the complexity of the sample including the mixing of information from linear and circular anisotropy as well as depolarization in the Mueller-matrix elements. Similar to beetle cuticle, right-handed circularly polarized light is transmitted in a band around 555 nm as seen in the elements m_{41} and m_{14}.

However, the central four elements indicate more complexity than a single circular Bragg resonance. Lower peaks and wider bands in the resonances in m_{41} and m_{14} compared to those in the beetle cuticle indicate qualitatively that the chiral domains in the CNC film exhibit a larger distribution in pitch than in the cuticle. The sample also exhibits linear anisotropy as seen in elements m_{43}, m_{34}, m_{42}, and m_{24} and is classified as bianisotropic.
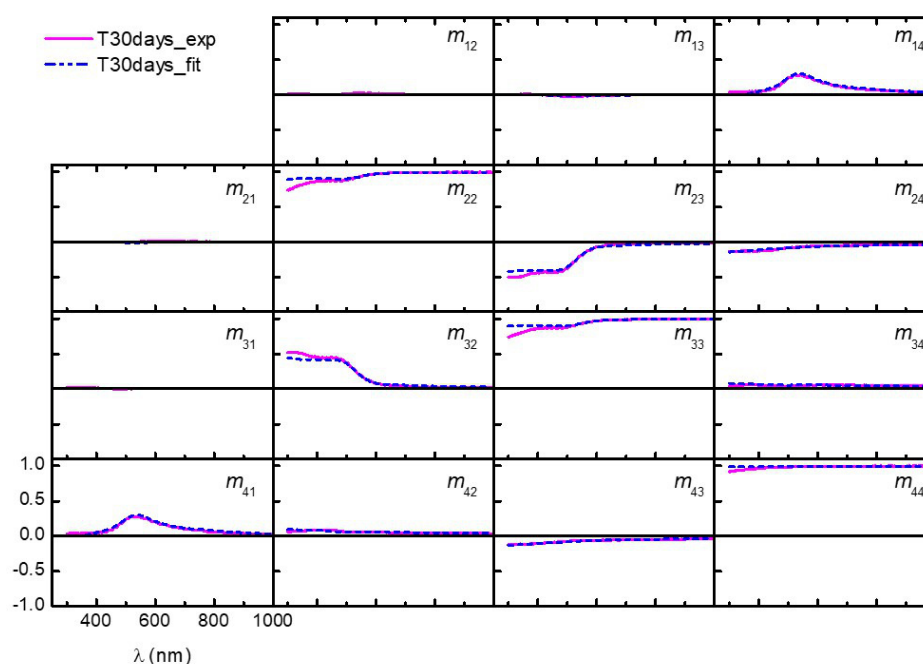

Figure 13. The transmission Mueller matrix of a 20 μm cellulose nanocrystal film (solid curves). The dashed curves shows the best model fit obtained with non-linear regression.

4.5.2. Method II

The bianisotropic effects of the CNC film can be quantified by using a differential decomposition with results as shown in Figure 14. The circular dichroism of the CNC film shows a resonance behavior, whereas the corresponding circular birefringence levels out at a close to constant level in the spectral region below the resonance. The linear effects are small and are dominated by L_B and L'_B, whereas L_D and L'_D are very close to zero.

Furthermore, L_B and L'_B are of similar shape and magnitude indicating that the in-plane optic axes of the CNC film are close to $\pi/8$. The oscillations seen most clearly in C_B and C_D are due to film thickness interference effects and are a sign of low absorption confirming the small values of L_D and L'_D. The depolarization of the CNC film is shown in Figure S4 in the Supplementary Materials.
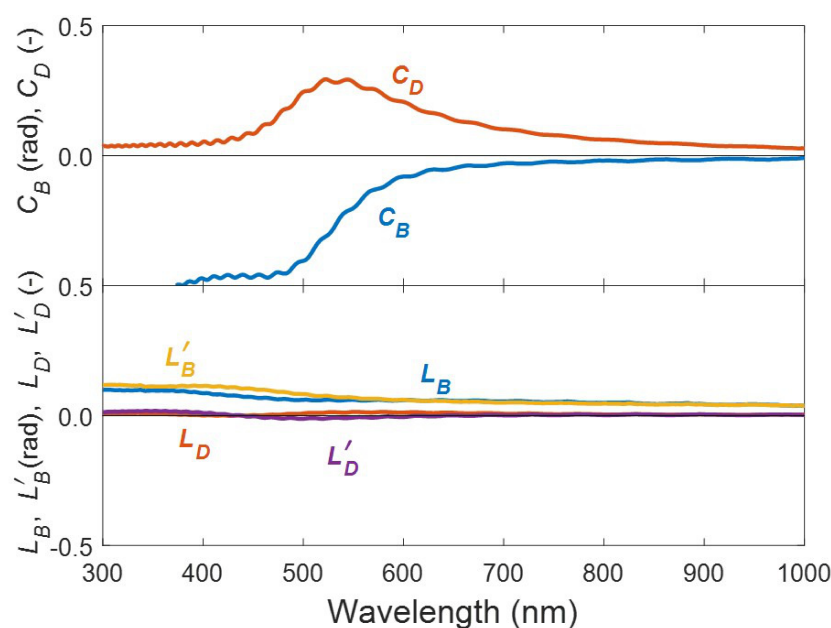
Figure 14. Birefringence and dichroism of the cellulose nanocrystal film determined by differential decomposition of the experimental data in Figure 13.

4.5.3. Method III

The chirality parameter $\kappa = \kappa_{\mathrm{Re}} + i\kappa_{\mathrm{Im}}$ and the refractive indices $n_{x'}$ and $n_{y'}$ in Equation (12) were fitted in a single layer model with film thickness of 20 μm and with dispersion models for the optical functions. Two Gaussian resonances were used for κ according to Equation (16) with the best-fit parameter values as shown in Table 4. Linear anisotropy was fitted using Cauchy models for n_x and for n_y similar to that in Equation (15), but with only three terms.

The cellulose material had low absorption, and linear dichroism was not included in the fit. The best-fit Cauchy parameters found were $A_{x'} = 1.57650 \pm 0.00002$, $A_{y'} = 1.57608 \pm 0.00002$, $B_{x'} = B_{y'} = 0.0034 \pm 0.0003$ μm², and $C_{x'} = C_{y'} = -0.00034 \pm 0.00001$ μm⁴. Due to the small birefringence, the B_j and C_j terms were set equal for the x' and y' directions. The linear birefringence found was, thus, wavelength independent and equal to $\Delta n_{x'y'} = A_{x'} - A_{y'} = 0.00042$. The origin of the linear birefringence may be density or orientation effects leading to a small in-plane linear anisotropy.

The reference axes x and y of the instrument are not aligned with the sample reference axes x' and y', and a Euler rotation angle ϕ is included in the fit. A value $\phi = 23.7°$ was found, which is in accordance with the $\pi/8$ estimate found using method II. The best model fit is shown in Figure 13, and Figure 15 presents the model chirality parameter κ of the CNC film.

Table 4. The Gaussian parameters for κ (offset $\kappa_0 = -0.000453 \pm 0.000002$) for the CNC film.

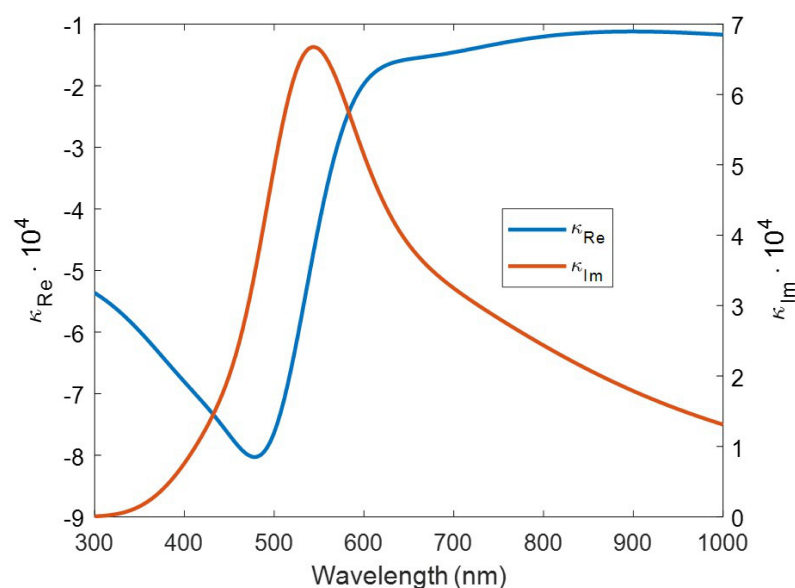| Resonance	A_j (-)	E_{0j} (eV)	Γ_j (eV)
1	0.000364 ± 0.000005	2.071 ± 0.005	1.37 ± 0.01
2	0.000329 ± 0.000005	2.304 ± 0.002	0.446 ± 0.008

Figure 15. Model function with two Gaussian resonances for the chirality parameter κ of the CNC film.

5. Discussion

The results obtained directly from a Mueller matrix (method I) may be considered as primary data. The only filtering is noise reduction depending on the data acquisition time chosen during the measurements. Values of C_B and C_D or the derived properties α and ϵ, respectively, may, therefore, be affected by instrument noise and systematic errors. This also holds for the differential decomposition approach (method II); however, as evaluation is done on the logarithm of a Mueller matrix, noise and systematic errors will propagate and, thereby, will be weighted differently compared to the original Mueller matrix.

In method III, a nonlinear regression is performed on the Mueller matrix elements using dispersion functions for the spectral variation in the materials properties. The values of these functions, which constitute the results of the analysis, are noise free, which means strong filtering. Depending on the function chosen, this may imply that small features in the data are missed. Systematic errors from the system as well as from model mismatch may, in addition, introduce false information in the results.

The example on a glucose solution should be considered as a demonstration on a simple case and not to promote the use of MMSE instead of polarimetry. Polarimetry is a very mature technique and has a resolution of the order of $\pm 0.01°$ or better in the polarization angle rotation α as found on vendor sites. Low-cost instruments with a resolution of $\pm 0.003°$ were presented [33]. In our results, we have an estimated resolution of $\pm 0.02°$ determined from the noise level in α in an MMSE measurement with a 10 s acquisition time. However, no efforts have been made to determine the attainable accuracy.

We used a medium precision balance and an ordinary measuring glass to prepare the glucose solution. For the rather high concentrations used, a concentration adjustment of $[\alpha]_{589}^{20}$ [34] should be made. Furthermore, the sodium D-line used is a doublet, and it makes some difference if $\lambda = 589.0$ or 589.6 nm is used. However, the specific rotations of 52.5, 52.5, and 52.0 obtained with methods I, II, and II, respectively, are surprisingly close to the data-base value $[\alpha]_{589}^{20} = +52.7$ [deg dm^{-1} cm^3 g^{-1}] [34].

The spectral variation of κ is complex as it may arise from various chemical groups in the glucose molecule as discussed by Listowski et al. [35]. Penzkofer used a Drude-type dispersion model to account for resonances in the ultraviolet spectral region. We found it sufficient to use a Cauchy model but with four terms to account for the complexity due to overlapping CB features from different subgroups. Penzkofer detected small CB features below 300 nm [36], which, however, could not be seen in our data.

If a sample only has CB and/or CD, it is not necessary to measure a complete Mueller matrix. Figure 16 shows an example of a measurement on the same D-glucose solution as in Figure 1 using a rotating analyzer ellipsometer with a fixed compensator. This type of instrument only records three rows of a Mueller matrix. From m_{23} and m_{32}, we can determine the specific rotation in a similar way as in Section 3.1, and we find, at $\lambda = 589$ nm, that $[\alpha]_{589}^{20} = +52.5$ [deg dm^{-1} cm^3 g^{-1}]. It is also possible to use symmetry conditions to expand a non-depolarizing Mueller matrix with three rows to a full Mueller matrix [6].
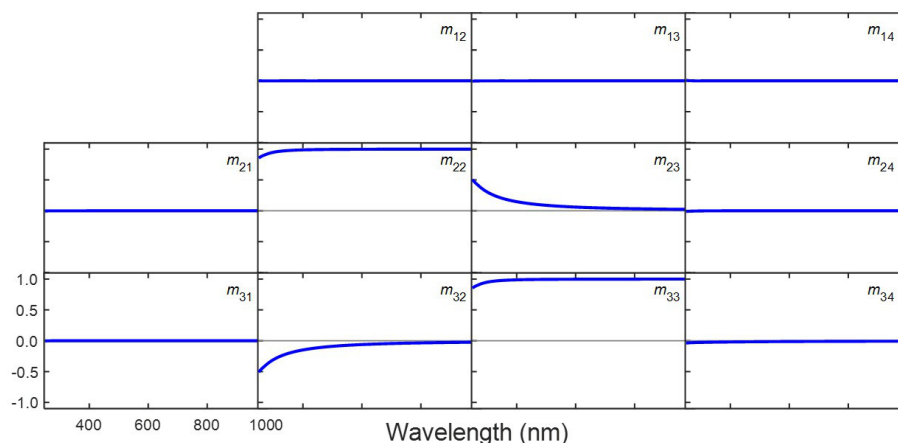

Figure 16. Partial Mueller matrix measured on a D-glucose solution using a rotating analyzer/fixed compensator spectroscopic ellipsometer.

In Method II, the natural logarithm of an experimental Mueller matrix is calculated. This corresponds to a transformation of experimental data, from measured transmission properties in terms of Mueller matrix elements to fundamental optical properties (C_B, C_D etc.) of the sample, but without distortion except for filtering if used. An alternative method to determine these properties is analytic inversion of a Muller matrix as suggested by Arteaga and Canillas [13]. This method also requires a homogeneous sample; however, in addition, the sample is non-depolarizing with a so-called Mueller–Jones matrix.

We only discussed natural and structural optical activity manifested as occurrences of CB and/or CD. In the presence of a quasistatic magnetic field, we may also observe similar effects, referred to as the Faraday effect, when the magnetic field is along the optical path. More generally, it is called the optical Hall effect and has been reviewed by Schubert et al. [37]. However, the birefringence and dichroic effects then arise from the breaking of symmetry in the permittivity tensor and are not contained in the chirality tensor.

The use of MMSE for studies of optical activity is a valuable complement to methods for the direct determination of spectral CB and CD properties. However, the recording of a normalized Mueller matrix is more complex as its 15 parameters are determined instead of a single parameter like a rotation angle in ORD or ellipticity in CD spectroscopy. In MMSE, compromises are made to assure precision in all elements as compared to the high resolution and accuracy obtainable in ORD and CD spectroscopy.

An ORD instrument is referred to as a polarimeter and is based on measuring changes in the direction of polarization, whereas, in CD-spectroscopy, a dichrometer measures changes in ellipticity. Modulation techniques are, thereby, employed, including photoelastic modulators and lock-in amplifiers to enhance the resolution and signal to noise ratio [38,39]. However, the fundamental properties measured, i.e., polarization changes, are the same in MMSE, ORD, and CD with the difference that MMSE in addition allows depolarization to be monitored.

The lower resolution of an ellipsometer compared to a polarimeter or a dichrometer with available instruments is, therefore, not a principle limitation but purely technical. Accordingly, in ORD and CD spectroscopy, it is implied that neither linear effects nor depolarization are present in the studied specimen. Consequently, incorrect values of unpredictable error magnitude for CD and CB will be reported if these effects cannot be

ignored. Therefore, MMSE can be seen as a generalization of the established methods to study chirality.

In cases when Mueller-matrices are used, a major advantage is that access to both C_B and C_D makes it possible to check the Kramers–Kronig consistency. Another advantage is that samples with depolarization can be addressed. With differential decomposition (method II), the depolarization properties are separated from the bianisotropic properties and can also be analyzed. In electromagnetic modeling (method III), it is possible to address small to medium depolarization by smearing, i.e., by assigning a distribution of parameters during modeling.

With methods I and II, as well as with ORD and CD spectroscopy, average sample properties are obtained, whereby it is assumed that samples are homogeneous along the optical path. As discussed above, linear effects may distort the results in method I, whereas isotropic effects do not interfere as long as the absorption is sufficiently low to obtain enough light throughput. However, if a sample is structured, e.g., has a layered structure, methods I and II fail to deliver correct results, but method III may still be applicable. In reflection mode, MMSE is routinely used with the electromagnetic modeling of structured samples, and layer thicknesses and permittivity tensors can be determined [40].

Such procedures are also applied in transmission mode although less common. In reflection mode, the extended constitutive relations used in method III are rarely used as the magnetoelectric tensors $\boldsymbol{\xi}$ and $\boldsymbol{\zeta}$ normally are to small to resolve. However, applications are found in transmission mode if sufficient optical path length can be achieved [6,7,11]. In the future, we will probably see more advanced applications addressing optical activity in several layers in a multilayered structure.

6. Concluding Remarks

The evaluation of optical activity using Mueller matrices is a valuable complement to ORD and CD spectrosocpy. Access to all 15 elements of a normalized Mueller matrix makes it possible to determine both circular birefringence and circular dichroism for a Kramers–Kronig consistency check. Furthermore, linear and circular anisotropic effects can be separated, and samples that exhibit depolarization can be studied. Finally, with electromagnetic modeling, individual chiral layers in multilayered samples can be characterized.

Abbreviations

The following abbreviations are used in this manuscript:

MDPI   Multidisciplinary Digital Publishing Institute
DOAJ   Directory of open access journals
CNC   Cellulose nanocrystals
MMSE   Mueller-matrix spectroscopic ellipsometry
LD   Linear dichroism
LB   Linear birefringence
CD   Circular dichroism
CB   Circular birefringence
CA   *Cetonia aurata*
ChGLC   Cholesteric glassy liquid crystal
KK   Kramers–Kronig transform
ORD   Optical rotatory dispersion

Appendix A

Appendix A.1. Conventions

Unfortunately, different conventions have been established in different fields of science. Of special importance in this communication is the convention for time dependence in field quantities. The time dependence can either be expressed as $e^{i\omega t}$ or $e^{-i\omega t}$ as both are allowed in plane wave solutions of Maxwell's equations. In the ellipsometry community, the $e^{i\omega t}$ (engineering) convention is dominating [3,41,42], likely, as this field has its roots in an electrical engineering community. In other areas of optics, it varies and both $e^{i\omega t}$ [12,43,44] and $e^{-i\omega t}$ [1,45–48] are used and sometimes both [49]. To make a comparison easier between the fields of ellipsometry and circular dichroism as well as circular birefringence, we include both conventions in the expressions discussed.

There are also variations in which order the difference in index for birefringence and dichroism is defined. Here, we use the order as defined in Table 1.

Ambiguity is also found due to the direction of viewing (towards the source or towards the detector) when defining handedness and a positive direction of the polarization azimuth. In this report, left-handed polarization corresponds to when the field vector rotates counter-clockwise when looking towards the source, and the polarization azimuth is counted from the x-axis and positive in the counter-clockwise direction.

The parameters for CB and CD are defined in Section 3 using the convention with time dependence $e^{-i\omega t}$. With the convention $e^{i\omega t}$, the definitions will be $C = C_{\mathrm{B}} - iC_{\mathrm{D}}$, $L = L_{\mathrm{B}} - iL_{\mathrm{D}}$, and $L' = L'_{\mathrm{B}} - iL'_{\mathrm{D}}$ as is used, e.g., in [11].

Appendix A.2. Mueller Matrix of a Circular Diattenuator

The Mueller matrix in Equation (3) can be derived from the circular Jones matrix of a circular diattenuator given by

$$\mathbf{J}_{\mathrm{D}}^{\mathrm{lr}} = \begin{bmatrix} e^{-\frac{2\pi d}{\lambda}k_{\mathrm{l}}} & 0 \\ 0 & e^{-\frac{2\pi d}{\lambda}k_{\mathrm{r}}} \end{bmatrix}, \tag{A1}$$

where the superscript lr indicates the use of circular Jones basis vectors. Conversion to Cartesian (xy) Jones basis vectors are performed according to [14]

$$\mathbf{J}_{\mathrm{D}}^{\mathrm{xy}} = \mathbf{F}\mathbf{J}^{lr}\mathbf{F}^{-1} = \frac{1}{2} \begin{bmatrix} 1 & 1 \\ -i & i \end{bmatrix} \begin{bmatrix} e^{-\frac{2\pi d}{\lambda}k_{\mathrm{l}}} & 0 \\ 0 & e^{-\frac{2\pi d}{\lambda}k_{\mathrm{r}}} \end{bmatrix} \begin{bmatrix} 1 & i \\ 1 & -i \end{bmatrix} =$$
$$e^{-\frac{2\pi d}{\lambda}\frac{(k_{\mathrm{l}}+k_{\mathrm{r}})}{2}} \begin{bmatrix} \cosh C_{\mathrm{D}}/2 & -i\sinh C_{\mathrm{D}}/2 \\ i\sinh C_{\mathrm{D}}/2 & \cosh C_{\mathrm{D}}/2 \end{bmatrix}. \tag{A2}$$

Finally, $\mathbf{M}_D$ in Equation (3) is obtained by the Jones to Mueller conversion $\mathbf{M} = \mathbf{A}(\mathbf{J} \otimes \mathbf{J}^*)\mathbf{A}^{-1}$ where $\otimes$ is the Kronecker product and [14]

$$
\mathbf{A} = \begin{bmatrix} 1 & 0 & 0 & 1 \\ 1 & 0 & 0 & -1 \\ 0 & 1 & 1 & 0 \\ 0 & i & -i & 0 \end{bmatrix} \quad \mathbf{A}^{-1} = \frac{1}{2} \begin{bmatrix} 1 & 1 & 0 & 0 \\ 0 & 0 & 1 & -i \\ 0 & 0 & 1 & i \\ 1 & -1 & 0 & 0 \end{bmatrix}. \tag{A3}
$$

Equation (A1) is independent of conventions for time dependence ($e^{-i\omega t}$ or $e^{+i\omega t}$), which holds also for Equation (3).

Appendix A.3. Relation between C_D and Ellipticity Angle ϵ

For elliptically polarized light, the ellipticity is defined as $e = b/a$ where a and b are the major and minor axes of the polarization ellipse [14]. The ellipticity angle $\epsilon = \arctan e$ is also in use. The relation between C_D and e can be found by using Jones formalism. If an incident linearly x-polarized light with a Jones vector $\mathbf{E} = [1,0]^T$ propagates through a circular dichroic sample with a Jones matrix from Equation (A2), the emerging Jones vector will be

$$
\mathbf{J}^{out} = \begin{bmatrix} E_x \\ E_y \end{bmatrix} = e^{-\frac{2\pi d}{\lambda}\frac{(k_1+k_r)}{2}} \begin{bmatrix} \cosh C_D/2 & -i\sinh C_D/2 \\ i\sinh C_D/2 & \cosh C_D/2 \end{bmatrix} \begin{bmatrix} 1 \\ 0 \end{bmatrix} =
$$
$$
e^{-\frac{2\pi d}{\lambda}\frac{(k_1+k_r)}{2}} \begin{bmatrix} \cosh C_D/2 \\ i\sinh C_D/2 \end{bmatrix}. \tag{A4}
$$

The ellipticity is calculated from $e = \Im[E_y]/\Re[E_x]$ and is

$$
e = \tan\epsilon = \tanh C_D/2. \tag{A5}
$$

In CD-spectroscopy, the difference in absorbance $\Delta A = A_1 - A_r$ is measured. Here, A_1 and A_r are the absorbance for left-handed and right-handed polarization, respectively. The Jones vector in Equation (A2) can be reformulated as

$$
\begin{bmatrix} E_x \\ E_y \end{bmatrix} = \frac{1}{2} \begin{bmatrix} e^{-\frac{2\pi d}{\lambda}k_1} + e^{-\frac{2\pi d}{\lambda}k_r} \\ -i(e^{-\frac{2\pi d}{\lambda}k_1} - e^{-\frac{2\pi d}{\lambda}k_r}) \end{bmatrix} = \frac{1}{2} \begin{bmatrix} \sqrt{T_1} + \sqrt{T_r} \\ -i(\sqrt{T_1} - \sqrt{T_r}) \end{bmatrix}, \tag{A6}
$$

and the definition of ellipticity used in CD-spectroscopy follows

$$
e = \tan\epsilon = \frac{\sqrt{T_r} - \sqrt{T_1}}{\sqrt{T_r} + \sqrt{T_1}}. \tag{A7}
$$

Beer–Lamberts law $T = 10^{-A} = e^{-A\ln 10}$ implies that $\sqrt{T} = e^{-\frac{A}{2}\ln 10}$ and

$$
\begin{bmatrix} E_x \\ E_y \end{bmatrix} = \frac{1}{2} \begin{bmatrix} e^{-\frac{A_1}{2}\ln 10} + e^{-\frac{A_r}{2}\ln 10} \\ -i(e^{-\frac{A_1}{2}\ln 10} - e^{-\frac{A_r}{2}\ln 10}) \end{bmatrix} = \frac{e^{-\frac{A_r}{2}\ln 10}}{2} \begin{bmatrix} e^{-\frac{\Delta A}{2}\ln 10} + 1 \\ -i(e^{-\frac{\Delta A}{2}\ln 10} - 1) \end{bmatrix} \tag{A8}
$$

from which the full expression for e expressed in ΔA becomes

$$
e = \tan\epsilon = -\frac{e^{-\frac{\Delta A}{2}\ln 10} - 1}{e^{-\frac{\Delta A}{2}\ln 10} + 1}. \tag{A9}
$$

From this expression, we may also derive the relation between C_D and ΔA by using Equation (A5)

$$
C_D = \Delta A \ln 10. \tag{A10}
$$

In CD-spectroscopy, it is customary to assume small ΔA (small $e = \tan \epsilon \approx \epsilon$) and Equation (A9) reduces to the following relation in practical use

$$e \approx \epsilon \approx \frac{\Delta A}{4} \ln 10 \frac{180}{\pi} = 32.98 \Delta A \quad [\text{deg}] \tag{A11}$$

where the factor $180/\pi$ is a conversion from rad to degrees. Finally, we also find, from Equation (A5), that $e \approx C_\text{D}/2$ for small e and, thus,

$$C_\text{D} \approx 2\epsilon. \tag{A12}$$

*Appendix A.4. Effects of Choice of Time Dependence in the **L**-Matrix*

Various signs due to the choice of conventions are used by different authors in the **L**-matrix in Equation (9). We used the $e^{-i\omega t}$ convention and definitions of the anisotropic parameters as in Table 1. Derivations of a few of the elements of **L** are given here as examples. Further details are given by Azzam [3]. The starting point is the differential propagation matrix defining the matrix **m**

$$\mathbf{m} = \lim_{\Delta z \to 0} \frac{\mathbf{M}(z, \Delta z) - \mathbf{I}}{\Delta z} \tag{A13}$$

where $\mathbf{M}(z, \Delta z)$ is the Mueller matrix for propagation from z to $z + \Delta z$ in a homogeneous material. A linear xy retarder has the Mueller matrix

$$\mathbf{M} = \begin{bmatrix} 1 & 0 & 0 & 0 \\ 0 & 1 & 0 & 0 \\ 0 & 0 & \cos \delta_{xy} & \sin \delta_{xy} \\ 0 & 0 & -\sin \delta_{xy} & \cos \delta_{xy} \end{bmatrix}, \tag{A14}$$

where $\delta_{xy} = 2\pi d_\text{R}(n_x - n_y)/\lambda$ and d_R is the retarder thickness. For a thin slab ($z \to z + \Delta z$) with thickness Δz, we can expand cosine and sine as $\cos \delta_{xy} \approx 1$ and $\sin \delta_{xy} \approx \delta_{xy}$. Equation (A14) then results in the Mueller matrix

$$\mathbf{M}(z, \Delta z) \approx \begin{bmatrix} 1 & 0 & 0 & 0 \\ 0 & 1 & 0 & 0 \\ 0 & 0 & 1 & \delta \\ 0 & 0 & -\delta & 1 \end{bmatrix} = \begin{bmatrix} 1 & 0 & 0 & 0 \\ 0 & 1 & 0 & 0 \\ 0 & 0 & 1 & \eta \Delta z \\ 0 & 0 & -\eta \Delta z & 1 \end{bmatrix} \tag{A15}$$

where we introduced $\eta = 2\pi(n_x - n_y)/\lambda$. The matrix **m** for a linear xy retarder now follows from its definition in Equation (A13)

$$\mathbf{m} = \begin{bmatrix} 0 & 0 & 0 & 0 \\ 0 & 0 & 0 & 0 \\ 0 & 0 & 0 & \eta \\ 0 & 0 & -\eta & 0 \end{bmatrix}. \tag{A16}$$

Finally, we obtain the matrix **L** by multiplying with the sample thickness d, and, by also noting that $\eta d = L_\text{B}$, we obtain

$$\mathbf{L} = d\mathbf{m} = \begin{bmatrix} 0 & 0 & 0 & 0 \\ 0 & 0 & 0 & 0 \\ 0 & 0 & 0 & \eta d \\ 0 & 0 & -\eta d & 0 \end{bmatrix} = \begin{bmatrix} 0 & 0 & 0 & 0 \\ 0 & 0 & 0 & 0 \\ 0 & 0 & 0 & L_\text{B} \\ 0 & 0 & -L_\text{B} & 0 \end{bmatrix}. \tag{A17}$$

The retarder Mueller matrix for the $\pm 45°$ direction is

$$\mathbf{M} = \begin{bmatrix} 1 & 0 & 0 & 0 \\ 0 & \cos \delta_{\pm 45°} & 0 & -\sin \delta_{\pm 45°} \\ 0 & 0 & 1 & 0 \\ 0 & \sin \delta_{\pm 45°} & 0 & \cos \delta_{\pm 45°} \end{bmatrix},$$
(A18)

and with the same procedure as above, we find

$$\mathbf{L} = \begin{bmatrix} 0 & 0 & 0 & 0 \\ 0 & 0 & 0 & -L'_{\mathrm{B}} \\ 0 & 0 & 0 & 0 \\ 0 & L'_{\mathrm{B}} & 0 & 0 \end{bmatrix}.$$
(A19)

The diattenuator Mueller matrix for the *xy* direction is

$$\mathbf{M} = \begin{bmatrix} 1 & -\tanh L_{\mathrm{D}} & 0 & 0 \\ -\tanh L_{\mathrm{D}} & 1 & 0 & 0 \\ 0 & 0 & \sinh L_{\mathrm{D}} & 0 \\ 0 & 0 & 0 & \sinh L_{\mathrm{D}} \end{bmatrix},$$
(A20)

and with the same procedure as above, we obtain

$$\mathbf{L} = \begin{bmatrix} 0 & -L_{\mathrm{D}} & 0 & 0 \\ L_{\mathrm{D}} & 0 & 0 & 0 \\ 0 & 0 & 0 & 0 \\ 0 & 0 & 0 & 0 \end{bmatrix}.$$
(A21)

If the engineering convention is used, the signs of L_{D}, L'_{D} and C_{D} will not change in Equation (9), whereas the signs of L_{B}, L'_{B}, and C_{B} will change to the opposite.

References

1. Laurence, N.; Nafie, L. *Vibrational Optical Activity: Principles and Applications*; John Wiley & Sons: Hoboken, NJ, USA, 2011.
2. Go, N. Optical activity of anisotropic solutions. II. *J. Phys. Soc. Jpn.* **1967**, *23*, 88–97. [CrossRef]
3. Azzam, R.M.A. Propagation of partially polarized light through anisotropic media with or without depolarization: A differential 4x4 matrix calculus. *J. Opt. Soc. Am. A* **1978**, *68*, 1756–1767. [CrossRef]
4. Ossikovski, R. Differential matrix formalism for depolarizing anisotropic media. *Opt. Lett.* **2011**, *36*, 2330–2428. [CrossRef]
5. Arteaga, O.; Kahr, B. Characterization of homogenous depolarizing media based on Mueller matrix differential decomposition. *Opt. Lett.* **2013**, *38*, 1134–1136. [CrossRef] [PubMed]
6. Schulz, M.; Zablocki, J.; Brück, O.; Balzer, F.; Lützen, A.; Arteaga, O.; Schiek, M. Giant intrinsic circular dichroism of prolinol-derived squaraine thin films. *Nat. Commun.* **2018**, *9*, 2413. [CrossRef]
7. Arwin, H.; Mendoza-Galván, A.; Magnusson, R.; Andersson, A.; Landin, J.; Järrendahl, K.; Garcia-Caurel, E.; Ossikovski, R. Structural circular birefringence and dichroism quantified by differential decomposition of spectroscopic transmission Mueller matrices from Cetonia aurata. *Opt. Lett.* **2016**, *41*, 3293–3296. [CrossRef]
8. Mendoza-Galván, A.; E. Muñoz-Pineda, S.R.; Santos, M.; Järrendahl, K.; Arwin, H. Mueller matrix spectroscopic ellipsometry study of chiral nanocrystalline cellulose films. *J. Opt.* **2018**, *20*, 024001. [CrossRef]
9. Arwin, H.; Magnusson, R.; Järrendahl, K.; Schoeche, S. Effective structural chirality of beetle cuticle determined from transmission Mueller matrices using the Tellegen constitutive relations. *J. Vac. Sci. Techn. B* **2020**, *38*, 014004. [CrossRef]
10. Wallace, J.U.; Shestopalov, A.; Chen, S.H. Scalable Synthesis of Cholesteric Glassy Liquid Crystals. *Ind. Eng. Chem. Res.* **2018**, *57*, 4470–4473. [CrossRef]
11. Arteaga, O.; Kahr, B. Mueller matrix polarimetry of bianisotropic materials. *J. Opt. Soc. Am. B* **2019**, *36*, F72–F83. [CrossRef]
12. Colett, E. *Polarized Light Fundamentals and Applications*; Marcel Dekker: New York, NY, USA, 1993.
13. Arteaga, O.; Canillas, A. Measurement of the optical activity of anisotropic samples by transmission Mueller matrix ellipsometry. *EPJ Web Conf.* **2010**, *5*, 03001. [CrossRef]
14. Azzam, R.; Bashara, N. *Ellipsometry and Polarized Light*; North-Holland: Amsterdam, The Netherlands, 1986.
15. Mendoza-Galván, A.; Li, Y.; Yang, X.; Magnusson, R.; Järrendahl, K.; Berglund, L.; Arwin, H. Transmission Mueller-matrix characterization of transparent ramie films. *J. Vac. Sci. Technol. B* **2019**, *38*, 014008. [CrossRef]

16. Ishimaru, A.; Lee, S.W.; Kuga, Y.; Jandhyala, V. Generalized Constitutive Relations for Metamaterials Based on the Quasi-Static Lorentz Theory. *IEEE Trans. Antennas Propag.* **2003**, *51*, 2550–2557. [CrossRef]

17. Lekner, J. Optical properties of isotropic chiral media. *Pure App. Opt.* **1996**, *5*, 417–443. [CrossRef]

18. Weast, R.C. *Handbook of Chemistry and Physics*, 53rd ed.; CRC Press: Boca Raton, FL, USA, 1972.

19. Pye, J.D. The distribution of circularly polarized light reflection in the Scarabaeoidea (Coleoptera). *Biol. J. Linnean Soc.* **2010**, *100*, 585–596. [CrossRef]

20. Michelson, A.A. On metallic colouring in birds and insects. *Phil. Mag.* **1911**, *21*, 554–567. [CrossRef]

21. Lenau, T.; Barfoed, M. Colours and Metallic Sheen in Beetle Shells—A Biomimetic Search for Material Structuring Principles Causing Light Interference. *Adv. Eng. Mat.* **2008**, *10*, 299–314. [CrossRef]

22. Goldstein, D.H. Polarization properties of Scarabaeidae. *Appl. Opt.* **2006**, *45*, 7944–7950. [CrossRef]

23. Hodgkinson, I.; Lowrey, S.; Bourke, L.; Parker, A.; McCall, M. Mueller-matrix characterization of beetle cuticle: Polarized and unpolarized reflections from representative architectures. *Appl. Opt.* **2010**, *49*, 4558–4567. [CrossRef] [PubMed]

24. Arwin, H.; Magnusson, R.; Landin, J.; Järrendahl, K. Chirality-induced polarization effects in the cuticle of scarab beetles: 100 years after Michelson. *Philos. Mag.* **2012**, *92*, 1583–1599. [CrossRef]

25. del Fernández L.R.; Arwin, H.; Järrendahl, K. Polarization of Light Reflected from *Chrysina Gloriosa* Under Various Illuminations. *Mater. Proc.* **2014**, *1*, 172–176. [CrossRef]

26. Arwin, H.; Berlind, T.; Johs, B.; Järrendahl, K. Cuticle structure of the scarab beetle *Cetonia aurata* analyzed by regression analysis of Mueller-matrix ellipsometric data. *Opt. Expr.* **2013**, *21*, 22645–22656. [CrossRef] [PubMed]

27. Mendoza-Galván, A.; del Río, L.F.; Järrendahl, K.; Arwin, H. Graded pitch profile for the helicoidal broadband reflector and left-handed circularly polarizing cuticle of the scarab beetle *Chrysina chrysargyrea*. *Sci. Rep.* **2018**, *8*, 6456. [CrossRef] [PubMed]

28. Arwin, H.; Magnusson, R.; Garcia-Caurel, E.; Fallet, C.; Järrendahl, K.; Foldyna, M.; Martino, A.D.; Ossikovski, R. Sum decomposition of Mueller-matrix images and spectra of beetle cuticles. *Opt. Express* **2015**, *23*, 1951–1966. [CrossRef]

29. Chandrasekhar, S.; Prasad, J.S. Theory of Rotatory Dispersion of Cholesteric Liquid Crystals. *Mol. Cryst. Liq. Cryst.* **1971**, *14*, 115–128. [CrossRef]

30. Wang, J.; Lakhtakia, A.; Geddes, J.B. Multiple Bragg regimes exhibited by a chiral sculptured thin film half-space on axial excitation. *Optik* **2002**, *5*, 213–221. [CrossRef]

31. Faryad, M.; Lakhtakia, A. The circular Bragg phenomenon. *Adv. Opt. Photonics* **2014**, *6*, 225–292. [CrossRef]

32. de Vries, H. Rotatory Power and Other Optical Properties of Certain Liquid Crystals. *Acta Crystallogr.* **1951**, *4*, 219–226. [CrossRef]

33. Harvie, A.; Phillips, T.; deMello, J. A high-resolution polarimeter formed from inexpensive optical parts. *Sci. Rep.* **2020**, *10*, 5448. [CrossRef]

34. Maryadele, M.J.; Heckelman, P.E.; Koch, C.B.; Roman, K.J. *The Merck Index. An Encyclopedia of Chemicals, Drugs, and Biologicals*; Merck & Co., Inc.: Kenilworth, NJ, USA, 2006.

35. Listowsky, I.; Avigad, G.; England, S. Optical Rotatory Dispersion of Sugars. I. Relationship to Configuration and Conformation of Aldopyranoses. *J. Am. Chem. Soc.* **1965**, *87*, 1765–1771. [CrossRef]

36. Penzkofer, A. Optical Rotatory Dispersion Measurement of D-Glucose with Fixed Polarizer Analyzer Accessory in Conventional Spectrophotometer. *J. Anal. Sci. Meth. Instrum.* **2013**, *3*, 234–239. [CrossRef]

37. Schubert, M.; Khühne, P.; Darakchieva, V.; Hofmann, T. Optical Hall effect—Model description: tutorial. *J. Opt. Soc. Am. A* **2016**, *33*, 1553–1568. [CrossRef] [PubMed]

38. Shindo, Y. Application of polarized modulation technique in polymer science. *Opt. Eng.* **1995**, *34*, 3369–3384. [CrossRef]

39. Sutherland, J. Measurement of Circular Dichroism and Related Spectroscopies with Conventional and Synchrotron Light Sources: Theory and Instrumentation. In *Modern Techniques for Circular Dichroism and Synchrotron Radiation Circular Dichroism Spectroscopy*; Wallace, B.; Janes, R., Eds.; IOS Press: London, UK, 2009; pp. 19–72. [CrossRef]

40. Hertwig, A.; Esser, N.; Hinrich, K.; Beck, U. (Eds.) *Proceedings of the 7th International Conference on Ellipsometry*; Elsevier B.V.: Amsterdam, The Netherlands, 2017.

41. Fujiwara, H. *Spectroscopic Ellipsometry, Principles and Applications*; John Wiley & Sons, Ltd.: Hoboken, NJ, USA, 2007.

42. Muller, R. Definitions and conventions in ellipsometry. *Surf. Sci.* **1969**, *16*, 14–33. [CrossRef]

43. Cheng, D. *Field and Wave Electromagnetics*; Addison-Wesley Publishing Company, Inc.: Boston, MA, USA, 1989.

44. Cloude, S. *Polarization: Applications in Remote Sensing*; Oxford University Press: Oxford, UK, 2010.

45. Chen, H. *Theory of Electromagnetic Waves*; McGraw-Hill Book Company: New York, NY, USA, 1983.

46. Kittel, C. *Introduction to Solid State Physics*; John Wiley & Sons, Inc.: Hoboken, NJ, USA, 1976.

47. Pedrotti, F.; Pedrotti, L.; Pedrotti, L. *Introduction to Optics*; Pearson Prentice Hall: London, UK, 2007.

48. Cai, W.; Shalaev, V. *Optical Metamaterials: Fundamentals and Applications*; Springer: Berlin/Heidelberg, Germany, 2010.

49. Hecht, E. *Optics*; Addison Wesley: Boston, MA, USA, 2002.